Probabilistic Template of the Lateral Parabrachial Nucleus, Medial Parabrachial Nucleus, Vestibular Nuclei Complex, and Medullary Viscero-Sensory-Motor Nuclei Complex in Living Humans From 7 Tesla MRI

Kavita Singh[1]*, Iole Indovina[2,3], Jean C. Augustinack[4], Kimberly Nestor[4], María G. García-Gomar[1], Jeffrey P. Staab[5,6] and Marta Bianciardi[1]

[1] Brainstem Imaging Laboratory, Department of Radiology, Athinoula A. Martinos Center for Biomedical Imaging, Massachusetts General Hospital and Harvard Medical School, Boston, MA, United States, [2] Department of Medicine and Surgery, Saint Camillus International University of Health and Medical Sciences, Rome, Italy, [3] Laboratory of Neuromotor Physiology, IRCCS Santa Lucia Foundation, Rome, Italy, [4] Laboratory for Computational Neuroimaging, Department of Radiology, Athinoula A. Martinos Center for Biomedical Imaging, Massachusetts General Hospital and Harvard Medical School, Boston, MA, United States, [5] Department of Psychiatry and Psychology, Mayo Clinic, Rochester, MN, United States, [6] Department of Otorhinolaryngology – Head and Neck Surgery, Mayo Clinic, Rochester, MN, United States

The lateral parabrachial nucleus, medial parabrachial nucleus, vestibular nuclei complex, and medullary viscero-sensory-motor (VSM) nuclei complex (the latter including among others the solitary nucleus, vagus nerve nucleus, and hypoglossal nucleus) are anatomically and functionally connected brainstem gray matter structures that convey signals across multiple modalities between the brain and the spinal cord to regulate vital bodily functions. It is remarkably difficult to precisely extrapolate the location of these nuclei from *ex vivo* atlases to conventional 3 Tesla *in vivo* images; thus, a probabilistic brainstem template in stereotaxic neuroimaging space in living humans is needed. We delineated these nuclei using single-subject high contrast 1.1 mm isotropic resolution 7 Tesla MRI images. After precise coregistration of nuclei labels to stereotaxic space, we generated a probabilistic template of their anatomical locations. Finally, we validated the nuclei labels in the template by assessing their inter-rater agreement, consistency across subjects and volumes. We also performed a preliminary comparison of their location and microstructural properties to histologic sections of a postmortem human brainstem specimen. In future, the resulting probabilistic template of these brainstem nuclei in stereotaxic space may assist researchers and clinicians in evaluating autonomic, vestibular and VSM nuclei structure, function and connectivity in living humans using conventional 3 Tesla MRI scanners.

Keywords: lateral parabrachial nucleus, medial parabrachial nucleus, vestibular nuclei complex, solitary nucleus, vagus nerve nucleus, hypoglossal nucleus, *in vivo* neuroimaging-based human template, multi-contrast 7 Tesla MRI

INTRODUCTION

The lateral parabrachial (LPB) nucleus, medial parabrachial (MPB) nucleus, vestibular (Ve) nuclei complex and medullary viscero-sensory-motor (VSM) nuclei (i.e., solitary nucleus, vagus nerve nucleus, hypoglossal nucleus, prepositus, intercalated nucleus, and interpositus) complex are anatomically and functionally connected brainstem gray matter structures that convey signals across multiple modalities between the brain and the spinal cord to regulate vital bodily functions. Specifically, these structures, individually or synergistically, regulate arousal (e.g., LBP, MPB) (Kaur et al., 2013), gustatory processes (e.g., VSM) (Matsumoto, 2013), sensory-motor function (VSM) (Olszewski and Baxter, 1954), and autonomic functions like cardio-respiratory (e.g., LPB and MPB) (Damasceno et al., 2014) and gastrointestinal processes (e.g., VSM) (Bokiniec et al., 2017). Clinical conditions that alter the structure or function of these nuclei, including cerebrovascular events, autoimmune diseases, trauma, stroke (Choi and Kim, 2018) and neurodegenerative disorders may produce a wide variety of symptoms and signs including disruptions of sleep and alertness, autonomic dysregulation, vertigo, and impaired control of eye movements and gait.

To identify the location of arousal, vestibular and viscero-sensory-motor nuclei in living humans, neuroscientists and neurosurgeons currently rely on the work of neuroanatomists and pathologists, who created meticulous *postmortem* atlases of the human brainstem (Olszewski and Baxter, 1954; Paxinos and Huang, 1995; Naidich et al., 2009; Paxinos et al., 2012). Yet, it is remarkably difficult to precisely extrapolate the location of these nuclei from *ex vivo* atlases to conventional 3 Tesla *in vivo* images because these nuclei are not clearly visible in conventional imaging and display inter-subject and age-dependent variability. Moreover, *postmortem* atlases (Olszewski and Baxter, 1954; Paxinos and Huang, 1995; Naidich et al., 2009; Paxinos et al., 2012) are mostly *2D, non-probabilistic* (i.e., derived from a single or very few brainstem specimens —mostly of elderly subjects), and *non-deformable* (i.e., mostly static) representations of brainstem nuclei with inherent distortions due to tissue manipulation.

This indicates the need to expand current probabilistic neuroimaging brain atlases (Desikan et al., 2006; Destrieux et al., 2010; Bianciardi et al., 2015, 2018), to include these currently missing nuclei relevant for the aforementioned broad set of diseases.

The aim of this study was to create, in living humans, a stereotaxic probabilistic structural template of the right and left LPB (LPB-r and LPB-l), MPB (MPB-r and MPB-l), Ve (Ve-r and Ve-l), and VSM (VSM-r and VSM-l) using high-resolution (1.1-mm isotropic), multi-contrast diffusion fractional-anisotropy (FA) and T_2-weighted images at 7 Tesla. This tool may augment modern day research and clinical brainstem studies by enabling a more precise identification of the location of these nuclei in conventional 3 Tesla images of living humans.

MATERIALS AND METHODS

MRI Data Acquisition

To delineate LPB, MPB, Ve, and VSM nuclei we used data acquired in our previous study (Bianciardi et al., 2015), which is detailed below. After providing written informed consent in accordance with the Declaration of Helsinki, twelve healthy subjects (6m/6f, age 28 ± 1 years) underwent 7 Tesla MRI. The Massachusetts General Hospital Institutional Review Board approved the study protocol. Data were acquired using a custom-built 32-channel receive coil and volume transmit coil (Keil et al., 2010), which provided increased sensitivity for the brainstem compared to commercial coils. Common single-shot 2D echo-planar imaging (EPI) scheme was utilized to obtain 1.1 mm isotropic diffusion tensor images (DTI) in sagittal plane, and T_2-weighted images, with following parameters: matrix size/GRAPPA factor/nominal echo-spacing = 180 × 240/3/0.82 ms. The resulting T_2-weighted anatomical images and the DTI images had perfectly matched resolution and geometric distortions. The EPI scheme helped us overcome specific-absorption-rate limits of spin-warp T_2-weighted MRI at 7 Tesla. The additional parameters used for DTI and T_2-weighted image acquisition included: spin-echo EPI, echo-time/repetition-time = 60.8 ms/5.6 s, slices = 61, partial Fourier: 6/8, unipolar diffusion-weighting gradients (for DTI), number of diffusion directions = 60 (for DTI, b-value ∼ 1000 s/mm^2), 7 interspersed "b0" images (non-diffusion weighted, b-value ∼ 0 s/mm^2, also used as T_2-weighted MRI), 4 repetitions, acquisition time per repetition 6′43″. The entire acquisition time for T_2-weighted MRI and DTI was ∼ 27′. Importantly, for DTI acquisition at 7 Tesla, where tissue has shorter T_2 values, we used unipolar (Stejskal and Tanner, 1965) instead of bipolar (Reese et al., 2003) diffusion gradients. This led to shortened echo-time (less by ∼30 ms) and significantly improved sensitivity of high-resolution DTI.

MRI Data Pre-processing and Alignment to MNI Space

On a single-subject basis, after concatenation of four DTI repetitions, the data were preprocessed for distortion and motion artifacts using the Diffusion Toolbox in the FMRIB Software Library (FSL, Oxford, United Kingdom). The diffusion tensor at each voxel was estimated (using FRIMB's Diffusion toolbox) to compute diffusion tensor FA from tensor eigenvalues. After motion correction, affine transformation was performed to coregister the averaged 28 "b0" T_2-weighted images to DTI data (Bianciardi et al., 2015).

On a single-subject basis, precise coregistration of both T_2-weighted images and FA to MNI space was performed as in Bianciardi et al. (2015). Specifically, the brainstem of each subject was aligned to an MNI space based FA template (termed "IIT space"; Illinois Institute of Technology human brain atlas, v.3, Chicago, IL, United States) (Varentsova et al., 2014) using the Advanced Normalization Tool (ANTs, Philadelphia, PA, United States) (Avants et al., 2011). This template was used since it has high contrast, is compatible with

diffusion-based tractography and covers the whole brainstem (encompassing medulla as well). Particularly, we computed and concatenated a generic affine and a high-dimensional non-linear warp transformation of images with the same modality (FA maps). The generic affine transformation was calculated by concatenating center-of mass alignment (degrees of freedom- dof = 3), rigid (dof = 6), similarity (dof = 7), and fully affine (dof = 12) transformations with smoothing sigmas: 4, 2, 1, 0 voxels – fixed image space. The high-dimensional non-linear warp transformation employed histogram image matching prior to registration and a symmetric diffeomorphic normalization transformation model with smoothing sigmas: 3, 2, 1, 0 voxels – fixed image space. We also performed a cross correlation metric, gradient step size: 0.2; regular sampling, data winsorization – quantiles: 0.005, 0.995; four multi-resolution levels: shrink factors 6, 4, 2, 1 voxels – fixed image space; convergence criterion: slope of the normalized energy profile over the last 10 iterations $< 10^{-8}$. The resulting combined transformation (using a single-interpolation step method: linear), was then applied to both single-subject T_2-weighted and FA images. Further, for each subject, T_2-weighted and FA images were also aligned to MNI152 standard space (non-linear 6th generation MNI152_T1_1mm available for instance in FSL; coined "MNI152_1mm space"), which is a frequently utilized space for fMRI analysis. While the MNI152_1mm space and the IIT space show satisfactory alignment elsewhere, there is slight misalignment in the brainstem, particularly in the pons and medulla. As such, single-subject FA and T_2-weighted images were aligned to MNI152_1mm space. This was done by using a single-interpolation step (interpolation method: linear) and applying two concatenated transformations, namely single-subject to IIT space transformation (described above); and IIT to MNI152_1mm non-linear transformation, with parameters described above.

Single-Subject Labeling and Probabilistic Template Generation

On a single-subject basis, two raters (KS and MB) independently performed manual delineations (fslview, FSL, Oxford, United Kingdom) using multi-contrast FA maps and T_2-weighted images in IIT space to yield single-subject labels (i.e., masks) of the regions of interest (LPB-r/l, MPB-r/l, Ve-r/l, and VSM-r/l). The intersection of the labels of the two raters was used as the final label. Manual delineations were aided by the use of anatomical landmarks and neighborhood rules described in a literature postmortem brainstem atlas (Paxinos et al., 2012). Of note, to delineate each nucleus, we mainly used the image modality that displayed the nucleus boundaries with good contrast (FA MRI for LPB, MPB, Ve, VSM), and employed the other modality (T_2-weighted), which had poor contrast for that nucleus, to identify cerebrospinal fluid (CSF) boundaries (as for LPB and Ve nuclei).

A probabilistic neuroimaging template in IIT space was formulated for each nucleus as an average probability map of the nucleus label encompassing all subjects (100% overlap of nuclei labels across subjects, $n = 12$ was considered highest probability).

After registering the individual subject labels to MNI152_1mm space, by applying the IIT to MNI152 transformations described above (nearest neighbors interpolation), a similar template was derived in MNI152_1mm. We developed the resulting template (in both IIT and MNI152 spaces), to facilitate extrapolation to diffusion and functional MRI modalities.

For each subject and label (coregistered to single-subject native space via an inverse of the method described in section "MRI Data Pre-processing and Alignment to MNI Space") we also calculated the label volume in native space, yielding the mean standard error (SE) volume for all subjects and compared these values to literature (Paxinos et al., 2012) volumes as described in section "Template Validation."

Template Validation

The probabilistic nuclei template was validated by computing for each nucleus and subject: (i) the inter-rater agreement, as the modified Hausdorff distance between labels delineated by the two raters; (ii) the internal consistency across subjects of the final label, as the modified Hausdorff distance between each final label and the probabilistic template label (thresholded at 35%) generated by averaging the labels across the other 11 subjects (leave-one-out cross validation). For both the inter-rater agreement and the internal consistency, we calculated the modified Hausdorff distance (Dubuisson and Jain, 1994) which is a measure of spatial overlap frequently used in neuroimaging (Fischl et al., 2008; Klein et al., 2009, 2010; Augustinack et al., 2013). For each label, the minimum distance of every point on one label from the other label was averaged across all points, resulting in two distance values. The maximum value of these two values was calculated and used as modified Hausdorff distance. For each nucleus, the modified Hausdorff distance of (i) and (ii) was then averaged across subjects.

For further (iii) probabilistic template validation, we computed the volume of the delineated nuclei (i.e., of the final labels, intersection of the labels generated by each rater) and compared them to precisely computed literature nuclei volumes from the Paxinos atlas (Paxinos et al., 2012). For nuclei volume calculation based on the Paxinos atlas, we acquired snapshots of brainstem plates ranging from −5 to +32 mm (Figures 8.12–8.49 of Paxinos et al., 2012) using Adobe Acrobat Reader. Later each snapshot was converted to single-slice nifti images with a slice thickness of 1 mm and proper spatial resolution using Matlab. To determine the in-plane isotropic spatial resolution of each slice, the number of pixels between adjacent coordinates was computed manually based on coordinate system provided for each plate (Paxinos et al., 2012). This varied between 0.0222 and 0.0417 mm in the examined plates. Based on Paxinos nomenclature (Paxinos et al., 2012), we manually delineated using ITK-Snap (Yushkevich et al., 2006) sub-regions of LPB, MPB, Ve and VSM and combined them to obtain final nuclei. For MPB, based on Paxinos terminology, we combined MPB and MPB external part (MPBE). For LPB, based on Paxinos atlas, we combined sub-nuclei of LPB external (LPBE), LPB central (LPBC), LPB dorsal (LPBD), LPB, LPB-superior (LPBS), and LPB unlabeled (i.e., a very small neighboring region compatible with LPB, yet missing the LPB label in the Paxinos atlas).

We delineated and combined to final Ve nuclei complex the following Paxinos sub-nuclei: the nucleus of origin of vestibular efferents of the vestibular nerve (EVe), lateral vestibular nucleus (LVe), medial vestibular nucleus magnocellular part (MVeMC), medial vestibular nucleus (MVe), medial vestibular nucleus parvicellular part (MVePC), paravestibular nucleus (PaVe), spinal (i.e., inferior) vestibular nucleus (SpVe), and superior vestibular nucleus (SuVe). Similarly for VSM, we delineated and combined labels of: solitary nucleus commissural part (SolC), solitary nucleus dorsolateral part (SolDL), solitary nucleus dorsal part (SolD), solitary nucleus gelatinous part (SolG), solitary nucleus intermediate part (SolIM), solitary nucleus interstitial part (SolI), solitary nucleus medial part (SolM), solitary nucleus paracommissural part (SolPaC), solitary nucleus ventrolateral part (SolVL), solitary nucleus ventral part (SolV), vagus nerve nucleus (10N), hypoglossal nucleus (12N), prepositus (Pr), intercalated nucleus (In), and interpositus nucleus (IPo). To get a literature nucleus/sub-nucleus volume, we multiplied the number of delineated voxels in each nucleus/sub-nucleus by the voxel volume for each slice and added the resulting number across slices for each nucleus/subnucleus.

For additional (iv) validation of LPB and MPB probabilistic template labels, we performed preliminary histological evaluation of these nuclei in a postmortem human brainstem specimen. A brainstem specimen from a 65-year-old adult male without neurologic disease was obtained from MGH Autopsy Suite and studied. Five mesopontine transverse vibratome sections (50 μm thick) were Nissl (cell body) stained, and five adjacent sections were Gallyas (myelin) stained. Each section was mounted onto a gelatin dipped glass slide and dried overnight. _Nissl thionin-based staining:_ After defatting with chloroform-alcohol, and undergoing pre-treatment with acetic acid, sections were stained with 1% thionin for 3 min, differentiated in 70% with a few drops of glacial acetic acid, and dehydrated in ascending series (70, 70, 95, 95, 95, 100, and 100%) of alcohol. _Gallyas staining:_ Sections were post-fixed with 10% formol for 10 days. Then, they underwent the following steps: (1) _acetylation_ with 2:1 mixture of pyridine and acetic anhydride (30 min); (2) _wash_ with distilled water; (3) _impregnation_ with ammoniacal silver nitrate (pH 7.3, 30 min); (4) _wash_ with distilled water; (5) _development_ with stock ABC solutions of ammonium nitrate, sliver nitrate and tungstosilicic acid (10 min); (6) _development stop_ with 1% acetic acid; (7) _bleaching_ with 0.2% potassium ferricyanide (10 min); (8) _stop_ with 0.5% acetic acid; (9) _stop_ with 0.5% sodium thiosulfate; (10) _wash_ with distilled water; and (11) _dehydration_ with ascending series (50, 70, 95, and 100%) of alcohol. _Cover-slipping and digitization:_ After Nissl or Gallyas staining, sections were cover-slipped from xylene using Permount. The Nissl and Gallyas stained sections were digitized using an 80i Nikon Microscope (Microvideo Instruments, Avon, MA, United States) with a 4× objective (i.e., 40× total magnification), which resulted in images with a 1.85 μm pixel size. We automatically acquired the images using the virtual tissue workflow provided from Stereo Investigator (MBF Bioscience, Burli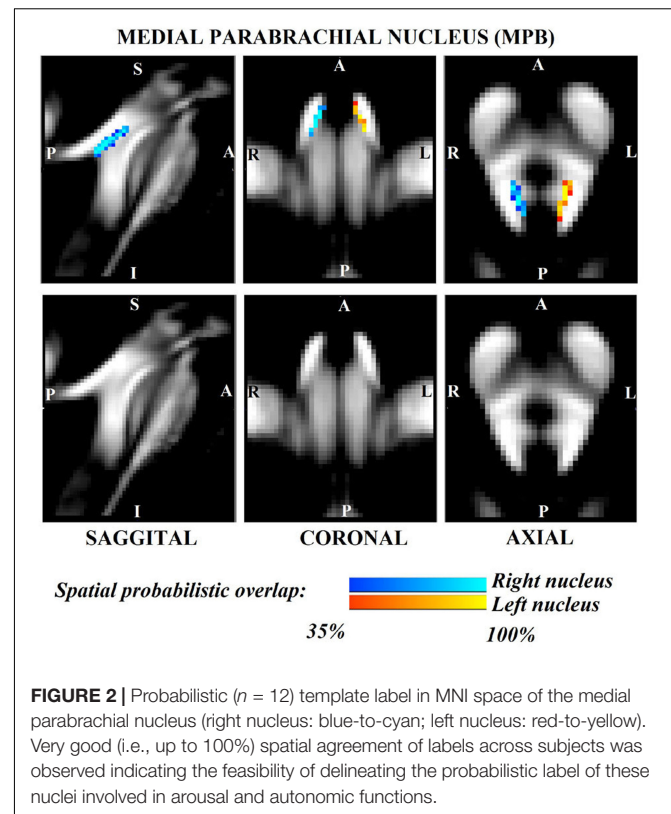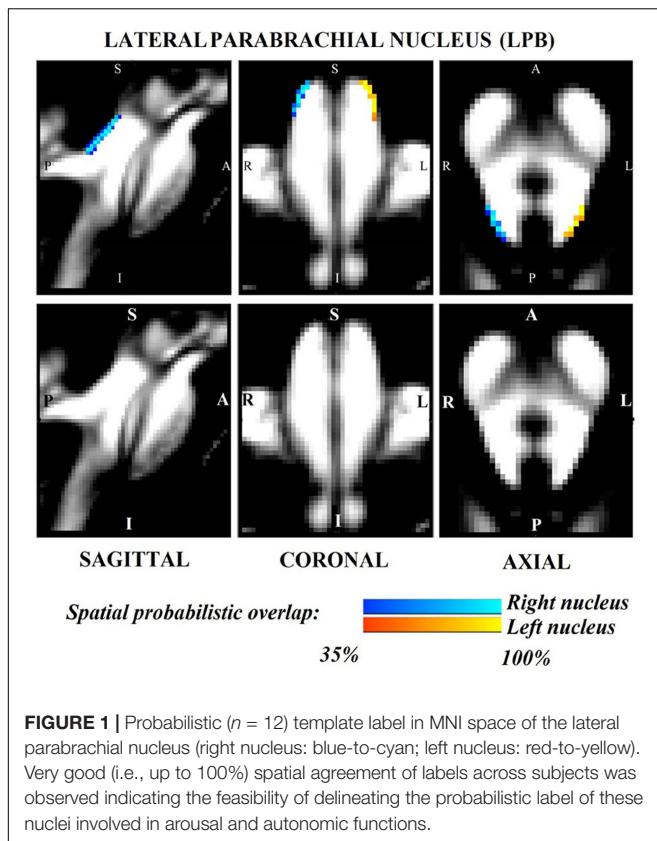ngton, VT, United States). Later we subtracted the background using GIMP[1], an open-source drawing and annotation software.

RESULTS

The probabilistic neuroimaging structural labels in MNI space of LPB-r/l, MPB-r/l, Ve-r/l, and VSM-r/l are shown in **Figures 1**–**4**. We briefly describe the nuclei delineations on the basis of the MRI contrast that guided them, as well as on the basis of neighborhood relationships with other visible structures. LPB (**Figure 1**) appeared as a thin hypointense region on FA maps at the mesopontine junction, bounded medially and ventro-medially by the superior cerebellar peduncle (SCP; a hyperintense region on FA maps), rostrally by the pedunculotegmental nucleus (a hypointense region on FA maps described in Bianciardi et al., 2018), and dorsally/dorsolaterally by the CSF (visible on T_2-weighted MRI). On FA maps, the MPB (**Figure 2**) was visible as a thin hypointense stripe lying along the medial surface of the SCP caudal to its decussation in the lateral part of the oral pontine tegmentum, and extending down to the level of oral pole of superior vestibular nucleus (described below). The superior, medial, lateral and spinal vestibular nuclei were not visible as individual nuclei, yet they appeared as a single hypointense oblong-shaped region on FA maps, which was labeled as Ve nuclei complex (**Figure 3**). This complex extended from the caudal tip of the MPB at the ponto-medullary junction, to the medulla at the level of the mid inferior olivary nucleus (a hypointense region in FA, delineated in our previous study (Bianciardi et al., 2015). On axial T_2-weighted images, this complex was bounded dorso-laterally by the CSF of the fourth ventricle (visible on T_2-weighted MRI). Finally, we delineated solitary along with nuclei 12N, 10N and smaller nuclei Pr, In, IPo within the VSM nuclei complex (**Figure 4**), an area of diffusion FA brighter than the adjacent medullary reticular formation and darker than neighboring white matter fiber bundles (e.g., medial longitudinal fasciculus). The VSM nuclei complex lay inferiorly to the ponto-medullary junction extending caudally throughout the medulla along the whole extent of the inferior olivary nucleus (hypointense region on FA images delineated in Bianciardi et al., 2015). On a coronal view, both VSM bilateral nuclei appeared as an inverted V-shape dorsally at their apex (**Figure 4**). Further, VSM assumed a lateral position in the floor of fourth ventricle in the periventricular medullary region. Orally, it lay next to Ve as a hypointense region, as seen in axial views of FA maps.

For each nucleus, the average modified Hausdorff distance assessing the inter-rater agreement and the internal consistency of nuclei template labels are shown in **Figure 5**. The modified Hausdorff distance and the internal consistency were found to be below ($p < 10^{-7}$ in unpaired one-tailed t-test) the linear spatial imaging resolution (1.1 mm), thus validating the generated probabilistic nuclei labels. Interestingly, we showed better values of inter-rater agreement (and the internal consistency, to a lesser extent) for Ve then LBP/MPB/VSM. This might be due to much bigger volume of Ve as opposed

---

[1]https://www.gimp.org

FIGURE 1 | Probabilistic (*n* = 12) template label in MNI space of the lateral parabrachial nucleus (right nucleus: blue-to-cyan; left nucleus: red-to-yellow). Very good (i.e., up to 100%) spatial agreement of labels across subjects was observed indicating the feasibility of delineating the probabilistic label of these nuclei involved in arousal and autonomic functions.

FIGURE 2 | Probabilistic (*n* = 12) template label in MNI space of the medial parabrachial nucleus (right nucleus: blue-to-cyan; left nucleus: red-to-yellow). Very good (i.e., up to 100%) spatial agreement of labels across subjects was observed indicating the feasibility of delineating the probabilistic label of these nuclei involved in arousal and autonomic functions.

to thin/smaller regions of LPB/MPB/VSM and very good contrast with respect to neighboring regions (e.g., white matter inferior cerebellar peduncle, ventricular CSF); however, nuclei volume should not be considered a limiting factor, and we found statistically significant values of inter-rater agreement and internal consistency in all nuclei.

The volume (mean ± SE across subjects) of each final label in native space and nuclei volumes from the literature (Paxinos et al., 2012) are shown in **Table 1**. The volume of MPB, Ve and VSM labels did not differ from Paxinos' volumes (*p*-value < 0.05), whereas the volumes of LPB were larger than volumes computed from the Paxinos atlas (Paxinos et al., 2012). In **Table 1**, we report details of volume computation of LPB, MPB, Ve, VSM nuclei and of nuclei sub-regions, as obtained from the Paxinos atlas and current study.

In **Figure 6**, we show a preliminary validation of the LPB and MPB *in vivo* nuclei label location and of their microstructural properties by the use of histology of a postmortem human brainstem specimen. Specifically, the FA map of MRI showed the hypointense region (as expected for gray matter nuclei) of LPB and MPB lining the hyperintense region of the SCP. Voxels of intermediate intensity in between SCP and parabrachial nuclei could be observed and could be attributed to partial volume effects. Nissl stain showed obvious difference between sparsely stained white matter of SCP and more densely stained gray matter of LPB and MPB displaying the distribution of neuronal cell bodies within these nuclei, further validating our nuclei localization. In the Gallyas staining, we found
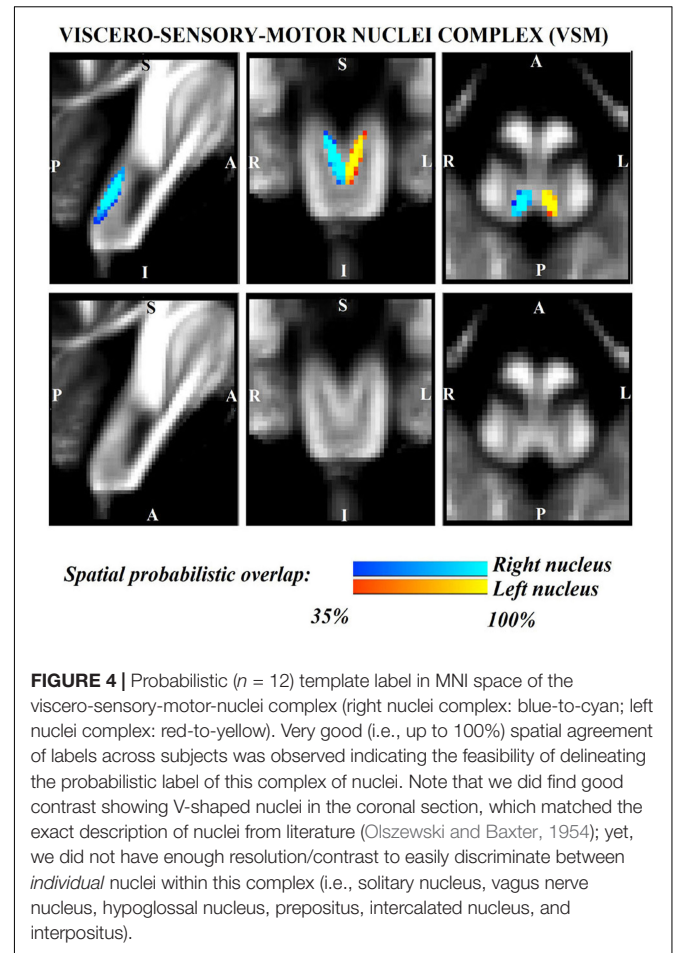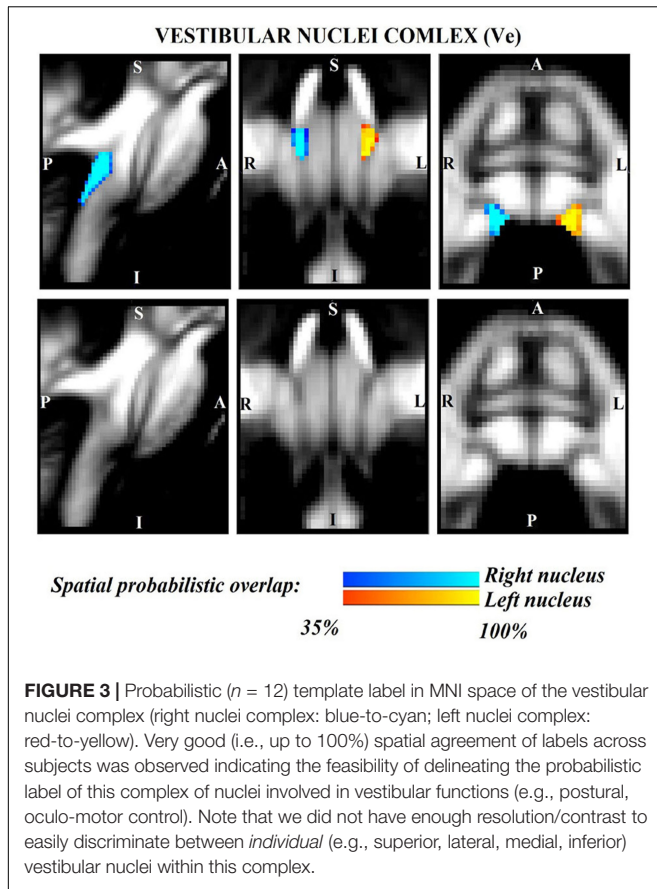
similar results where white matter of SCP could be demarcated from parabrachial nuclei based on their argyrophilic properties (**Figure 6**). These initial findings appear promising and need to be further extended for validation of Ve and VSM.

DISCUSSION

In the present work, we demonstrated the feasibility of single-subject delineations of LPB, MPB, Ve, and VSM nuclei in living humans using 7 Tesla MRI. Further, we created a probabilistic template of these nuclei after precise coregistration to stereotaxic neuroimaging space. Finally, we validated the generated template by assessing the inter-rater agreement, the consistency across subjects, and the volumes of the delineated labels. Our findings of most nuclei volumes match previously reported studies in literature (Paxinos et al., 2012), further strengthening our nuclei delineation. As a preliminary *ex vivo* validation, we performed histological staining of a few nuclei (LPB and MPB), which showed remarkable consistency to *in vivo* MRI. Here, we first discuss the strengths and limitations of nuclei delineations, then the nuclei function and the potential impact of the generated template.

Strengths and Limitations of Nuclei Delineations

We delineated LPB, MPB, Ve, and VSM nuclei based on high contrast FA maps and T$_2$−weighted images obtained at 7 Tesla. MRI acquisition at 7 Tesla as compared to 3 Tesla specifically

FIGURE 3 | Probabilistic (*n* = 12) template label in MNI space of the vestibular nuclei complex (right nuclei complex: blue-to-cyan; left nuclei complex: red-to-yellow). Very good (i.e., up to 100%) spatial agreement of labels across subjects was observed indicating the feasibility of delineating the probabilistic label of this complex of nuclei involved in vestibular functions (e.g., postural, oculo-motor control). Note that we did not have enough resolution/contrast to easily discriminate between *individual* (e.g., superior, lateral, medial, inferior) vestibular nuclei within this complex.

FIGURE 4 | Probabilistic (*n* = 12) template label in MNI space of the viscero-sensory-motor-nuclei complex (right nuclei complex: blue-to-cyan; left nuclei complex: red-to-yellow). Very good (i.e., up to 100%) spatial agreement of labels across subjects was observed indicating the feasibility of delineating the probabilistic label of this complex of nuclei. Note that we did find good contrast showing V-shaped nuclei in the coronal section, which matched the exact description of nuclei from literature (Olszewski and Baxter, 1954); yet, we did not have enough resolution/contrast to easily discriminate between *individual* nuclei within this complex (i.e., solitary nucleus, vagus nerve nucleus, hypoglossal nucleus, prepositus, intercalated nucleus, and interpositus).

provided better image sensitivity and resolution for nuclei delineations. The ~2.2 fold increase in sensitivity due to the higher field strength was further augmented by the use of a custom-built volume transmit coil and 32-channel receive coil (Keil et al., 2010). The latter provided improved sensitivity for

the brainstem compared to commercial coils with the same number of channels due to: (a) customized arrangement of the coil elements, also enabling a more efficient flip angle calibration
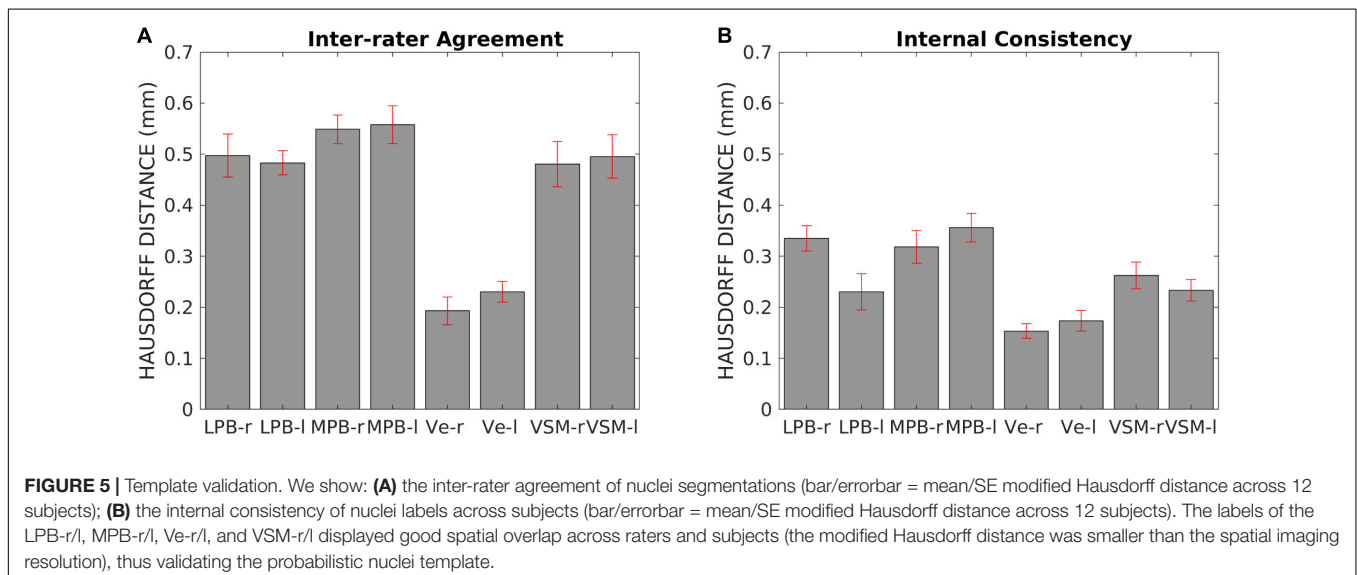

FIGURE 5 | Template validation. We show: **(A)** the inter-rater agreement of nuclei segmentations (bar/errorbar = mean/SE modified Hausdorff distance across 12 subjects); **(B)** the internal consistency of nuclei labels across subjects (bar/errorbar = mean/SE modified Hausdorff distance across 12 subjects). The labels of the LPB-r/l, MPB-r/l, Ve-r/l, and VSM-r/l displayed good spatial overlap across raters and subjects (the modified Hausdorff distance was smaller than the spatial imaging resolution), thus validating the probabilistic nuclei template.

TABLE 1 | Detailed computation of nuclei volumes from previous histology atlas (Paxinos et al., 2012) and from current study.

Nucleus name (acronym)	Sub-nucleus name (acronym)	Prior study (Paxinos et al., 2012)		Current study	
		Volume (mm^3)	Total volume (mm^3)	Right nucleus volume (mm^3)	Left nucleus volume (mm^3)
				Mean ± SE	Mean ± SE
Lateral parabrachial nucleus (LPB)	LPB	8.4	34.3	53.9 ± 2.6	54.7 ± 4.8
	LPB, central part (LPBC)	5.1			
	LPB, dorsal part (LPBD)	12.2			
	LPB, external part (LPBE)	2.5			
	LPB, unlabeled	6.1			
Medial parabrachial nucleus (MPB)	MPB	37.1	40.4	47.6 ± 3.8	46.3 ± 3.6
	MPB, external part (MPBE)	3.3			
Vestibular nuclei complex (Ve)	Nucleus of vestibular efferents (EVe)	0.5	136.4	135.5 ± 3.8	129.9 ± 4.0
	Lateral vestibular nucleus (LVe)	8.2			
	Medial vestibular nucleus (MVe)	35.9			
	MVe, magnocellular part (MVeMC)	6.2			
	MVe, parvicellular part (MVePC)	17			
	Paravestibular nucleus (PaVe)	3.7			
	Spinal vestibular nucleus (SpVe)	41.7			
	Superior vestibular nucleus (SuVe)	23.3			
Viscero-sensory-motor nuclei complex (VSM)	Solitary nucleus, commissural part (SolC)	1.8	90.6	84.9 ± 3.3	87.7 ± 3.2
	Sol, dorsolateral part (SolDL)	2.9			
	Sol, dorsal part (SolD)	0.2			
	Sol, gelatinous part (SolG)	4.4			
	Sol, intermediate part (SolIM)	6.6			
	Sol, interstitial part (SolI)	4.1			
	Sol, medial part (SolM)	5.9			
	Sol, paracommissural part (SolPaC)	1.4			
	Sol, ventrolateral part (SolVL)	1.7			
	Sol, ventral part (SolV)	1.7			
	Vagus nerve nucleus (10N)	11.8			
	Hypoglossal nucleus (12N)	19.1			
	Prepositus (Pr)	16.3			
	Intercalated nucleus (In)	6.4			
	Interpositus (IPo)	6.2			

for inferior areas of the brain; (b) sharp curvature posteriorly resembling human head and enabling better signal reception from the cerebellum and brainstem. To achieve optimized brainstem images at 7 Tesla it was also crucial to adopt: (i) minimum echo-time using monopolar scheme (given the lower gray and white matter T_2 values at higher magnetic field); (ii) optimized RF transmit gain in our region of interest (the brainstem), which was otherwise hindered by strong RF inhomogeneities at 7 Tesla, using actual flip angle imaging pulse sequence (Yarnykh, 2007); and (iii) semi-automatic B_0 shimming.

As expected from postmortem atlases, LPB bounded laterally and superiorly (in its most caudal aspect) the SCP, medially the CSF and inferiorly the pedunculotegmental nucleus. The MPB lay medial to the SCP, superior to vestibular nuclei and lateral to a gray matter area containing the locus coeruleus,

the laterodorsal tegmental nucleus and the central gray of the rhombencephalon. The superior, medial, lateral and spinal vestibular nuclei were not clearly visible as individual nuclei, yet as a complex with homogeneous FA. The Ve nuclei complex, in line with Paxinos atlas, extended from the caudal tip of the MPB at the ponto-medullary junction, to the medulla at the level of the mid inferior olivary nucleus; it was medial to the inferior cerebellar peduncle and ventral to the forth ventricle. Similarly, Sol, 12N, 10N and smaller nuclei Pr, In, IPo were delineated within the VSM nuclei complex, not individually. We observed a peculiar diffusion FA contrast of the VSM, which displayed intermediate FA values between neighboring gray matter, such as the medullary reticular formation, and white matter, such as the medial longitudinal fasciculus. We speculate that the partial volume effect of the VSM with the
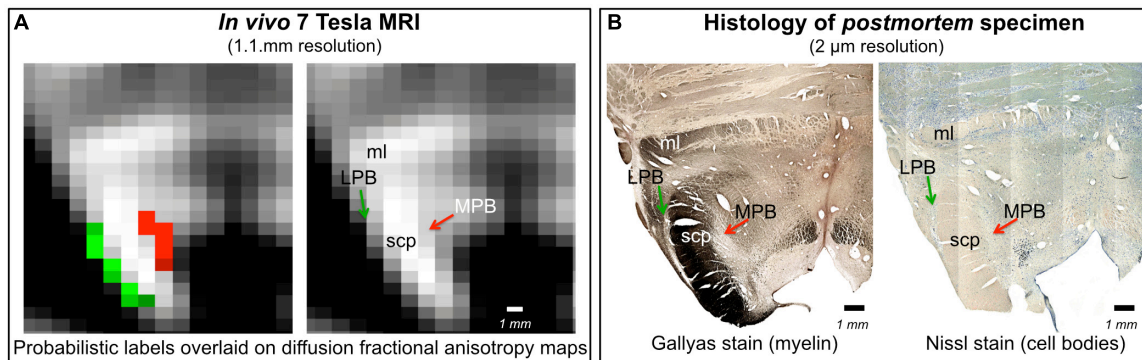
FIGURE 6 | *In vivo* nuclei template validation by preliminary histology of postmortem brainstem specimens. We provide further validation for the LPB and MPB brainstem nuclei delineations. As expected for gray matter regions, LPB and MPB were areas of: **(A)** hypointensity in *in vivo* 7 Tesla FA MRI maps; **(B)** hypointensity in myelin stains (left) and hyperintensity in cell body stains (right) of a postmortem brainstem specimen. In each panel, the LPB and MPB bounded, respectively, laterally and medially the white matter superior cerebellar peduncle (SCP; anterior to the SCP the medial lemniscus is labeled as ml).

solitary tract, nerves 10 and 12 might be at the origin of this contrast. In line with the Paxinos atlas (Paxinos et al., 2012), the VSM nuclei complex extended from the ponto-medullary junction, next to the Ve to the inferior medulla at a level of the lower tip of the inferior olivary nucleus, and was bounded dorsally by the CSF. Interestingly, on a coronal view, both VSM bilateral nuclei appeared as an inverted V-shape as described in other studies (Olszewski and Baxter, 1954; Naidich et al., 2009; Paxinos et al., 2012). These findings corroborated well with our histological evaluation (**Figure 6**), where we found similar anatomical landmarks for LPB and MPB as seen in our *in vivo* template. This postmortem evaluation was done in a cognitively healthy volunteer donor, who unfortunately did not undergo prior MRI evaluation. Thus, our validation was limited to a qualitative comparison for nuclei position, rather than a quantitative correlation of histology with *in vivo* MRI findings in the same subject. Note that, *in vivo* and *ex vivo* examination in same cognitively healthy adult volunteer are difficult to perform, especially in younger adults.

The quantitative validation using the inter-rater agreement and internal consistency of *in vivo* probabilistic labels provided positive results for all nuclei. The number of subjects in this study was limited; nevertheless, a sample size of 10–12 subjects was enough to achieve significant results in the current as well as previous brain/brainstem template work (Bianciardi et al., 2015, 2018; Croxson et al., 2018; García-Gomar et al., 2019). Comparison of the probabilistic label volume with the volume derived from the Paxinos histology-based atlas drawings (Olszewski and Baxter, 1954) was quite good for MPB, Ve, and VSM, yet there was some mismatch for LPB. We ascribe this discrepancy most probably to partial volume effects, because our LPB labels delineated using 1.1 mm isotropic resolution voxels might contain CSF and a stripe of the SCP adjacent to the LPB. The LPB is indeed a very thin stripe of gray matter with a width ranging between approximately 0.5 to 1 mm.

For proper applicability of this template, note that a precise coregistration to conventional MRI is needed. Nonetheless,

coregistration of subcortical structure is less trivial than coregistration of cortical foldings (Fischl et al., 2008; Greve and Fischl, 2009). Moreover, with the development of new registration tools (Klein et al., 2009; Avants et al., 2011) and of multi-modal atlases in MNI space (Varentsova et al., 2014) including diffusion-based contrast and T_2-weighted contrast, beyond the original MNI T_1-weighted contrast, we predict better accuracy of brainstem coregistration, for example from native single-subject space to MNI space. Same modality coregistration of single-subject images to target stereotaxic images has provided promising outcomes for single-subject FA maps to the IIT FA map, as used here. Recent work by our group has demonstrated the feasibility of generating a template in MNI space and functional connectome of tiny brainstem structures, thus proving the feasibility of accurately coregistering these small nuclei across subjects to a common template.

On the Nuclei Function and the Potential Impact of the Generated Template

We delineated LPB and MPB nuclei located at the mesopontine junction and involved in chemoreception, nociception, stress, autonomic control, aversive behaviors and arousal functions (Spector, 1995; Bester et al., 1997; Reilly and Trifunovic, 2001; Gauriau and Bernard, 2002; Chamberlin, 2004; Pattinson et al., 2009; Fuller et al., 2011; Kaur et al., 2013; Davern, 2014; Myers et al., 2017). For instance, functional studies (Pattinson et al., 2009; Zuperku et al., 2017) show the involvement of LPB and MPB nuclei in respiratory control; however, their roles could not be segregated due to unavailability of *in vivo* human atlas specifically delineating these labels at high-resolution (Pattinson et al., 2009). MPB relays information from the taste area of the solitary nucleus to the ventral posteromedial nucleus of the thalamus and forebrain (Sclafani et al., 2001; Naidich et al., 2009), while the LPB relays viscero-sensory information. Owing to multi-functional involvement of sub-nuclei of LPB and its overlapping role with MPB, we speculate our template might help in

refining definite roles for these nuclei in functional imaging in human subjects.

Brainstem vestibular and autonomic nuclei display an intricate wiring diagram with other brainstem nuclei and with the rest of the brain, as shown by animal and *ex vivo* work (Balaban, 2002; Balaban et al., 2011; Staab et al., 2013). Alteration in the connectivity of these nuclei is the hallmark of several brain disorders (Millan, 2002; Niblock et al., 2004; Brown et al., 2010; Linnman et al., 2012; Mello-Carpes and Izquierdo, 2013; Satpute et al., 2013), including vestibular disorders and anxiety (Balaban and Thayer, 2001; Balaban, 2004; Bächinger et al., 2019). According to the National Institutes of Health National Institute on Deafness and other Communication Disorders (NIDCD) (NIDCD, 2015), chronic vestibular disorders (including chronic imbalance and dizziness) affect about 5% of the American adult population, their mechanisms are not fully understood (Kitahara et al., 1997; Ris et al., 1997; Godemann et al., 2005; Heinrichs et al., 2007; Best et al., 2009; Dutia, 2010; Mahoney et al., 2013; Cousins et al., 2014) and treatment with serotonergic antidepressants and vestibular habituation are only partially successful (Staab et al., 2013). Adverse vestibular-autonomic interactions (Fischl et al., 2008; Indovina et al., 2014, 2015; Staab et al., 2014; Riccelli et al., 2017a,b; Nigro et al., 2018; Passamonti et al., 2018) appear to precipitate and perpetuate chronic vestibular disorders, crucially underlying the pathophysiologic process of these disorders. Our findings offer potential benefits to investigate the connectivity pathways of Ve and autonomic nuclei in living humans on widely available 3 Tesla scanners, and expand our knowledge of successful compensation for acute vestibular events versus development of chronic vestibular disorders.

Solitary nuclei integrate interoceptive and viscero-sensory input with descending affective and cognitive information from the limbic forebrain (Rinaman and Dzmura, 2007). Early studies showed solitary nuclei role in autonomic control, however recent literature indicates their involvement in plethora of behavioral and neuroendocrine processes (Rinaman, 2010), thereby further providing impetus for precise delineations of these nuclei in living humans. Solitary nuclei have been involved in behaviors relating to fear memory, anxiety and depression (Miyashita and Williams, 2002; Ghosal et al., 2014) along with modulating behavioral responses to stress, which is also governed by parabrachial nuclei. Based on these growing evidences of overlapping functions and differential response of these nuclei to stimuli and their mode of action, we advocate that the present study might help with nuclei localization and their future functional assessment, as well as facilitate the study of various neurological disorders and neurosurgical planning.

Summary, Conclusion, and Future Directions

In summary, we foresee that the generated probabilistic template of LPB, MPB, Ve, and VSM in stereotaxic space —representative of younger human adults— might be a useful tool for improving localization of brainstem nuclei involved in autonomic, vestibular and VSM functions. Researchers and clinicians will be able to shift from the difficult and imprecise task of extrapolating locations from *ex vivo* atlases to this new, user-friendly 3D, probabilistic, and deformable tool to identify the location of brainstem nuclei more precisely in *in vivo* images derived from conventional 3 Tesla MRI scanners. After its release on public repositories of neuroimaging data and tools, users will be able to precisely coregister the template onto single-subject 3 Tesla MRI, just as existing atlases [e.g., AAL, Harvard Oxford (Desikan et al., 2006; Destrieux et al., 2010)] are now used. This will make the template accessible to researchers and clinicians who use widely available 3 Tesla scanners, and study brainstem mechanisms in health, vestibular and balance disorders, impairment in autonomic and VSM function, sleep and anxiety disorders, as well as neurodegenerative disease.

DATA AVAILABILITY STATEMENT

The datasets analyzed in this article are not publicly available. Requests to access the datasets should be directed to martab@mgh.harvard.edu.

ETHICS STATEMENT

The studies involving human participants were reviewed and approved by MGH Institutional Review Board, Massachusetts General Hospital, Boston, MA, United States. The patients/participants provided their written informed consent to participate in this study.

AUTHOR CONTRIBUTIONS

MB designed the research, performed the experiments, and secured the funding in collaboration with II and JS. MB preprocessed and analyzed the *in vivo* data. KS and MB manually labeled the ROIs. MB, JA, and KN performed the histology. KS, II, KN, MG-G, JS, and MB wrote the manuscript. All authors gave feedback along the process.

FUNDING

REFERENCES

Augustinack, J. C., Huber, K. E., Stevens, A. A., Roy, M., Frosch, M. P., van der Kouwe, A. J. W., et al. (2013). Predicting the location of human perirhinal cortex, Brodmann's area 35, from MRI. *NeuroImage* 64, 32–42. doi: 10.1016/j.neuroimage.2012.08.071

Avants, B. B., Tustison, N. J., Song, G., Cook, P. A., Klein, A., and Gee, J. C. (2011). A reproducible evaluation of ANTs similarity metric performance in brain image registration. *NeuroImage* 54, 2033–2044. doi: 10.1016/j.neuroimage.2010.09.025

Bächinger, D., Luu, N.-N., Kempfle, J. S., Barber, S., Zürrer, D., Lee, D. J., et al. (2019). Vestibular aqueduct morphology correlates with endolymphatic sac pathologies in menière's disease-A correlative histology and computed tomography study. *Otol. Neurotol.* 40, e548–e555. doi: 10.1097/MAO.0000000000002198

Balaban, C. D. (2002). Neural substrates linking balance control and anxiety. *Physiol. Behav.* 77, 469–475. doi: 10.1016/s0031-9384(02)00935-6

Balaban, C. D. (2004). Projections from the parabrachial nucleus to the vestibular nuclei: potential substrates for autonomic and limbic influences on vestibular responses. *Brain Res.* 996, 126–137. doi: 10.1016/j.brainres.2003.10.026

Balaban, C. D., Jacob, R. G., and Furman, J. M. (2011). Neurologic bases for comorbidity of balance disorders, anxiety disorders and migraine: neurotherapeutic implications. *Expert Rev. Neurother.* 11, 379–394. doi: 10.1586/ern.11.19

Balaban, C. D., and Thayer, J. F. (2001). Neurological bases for balance-anxiety links. *J. Anxiety Disord.* 15, 53–79. doi: 10.1016/s0887-6185(00)00042-6

Best, C., Eckhardt-Henn, A., Tschan, R., and Dieterich, M. (2009). Psychiatric morbidity and comorbidity in different vestibular vertigo syndromes. Results of a prospective longitudinal study over one year. *J. Neurol.* 256, 58–65. doi: 10.1007/s00415-009-0038-8

Bester, H., Matsumoto, N., Besson, J. M., and Bernard, J. F. (1997). Further evidence for the involvement of the spinoparabrachial pathway in nociceptive processes: a c-Fos study in the rat. *J. Comp. Neurol.* 383, 439–458. doi: 10.1002/(sici)1096-9861(19970714)383:4<439::aid-cne4>3.3.co;2-n

Bianciardi, M., Strong, C., Toschi, N., Edlow, B. L., Fischl, B., Brown, E. N., et al. (2018). A probabilistic template of human mesopontine tegmental nuclei from in vivo 7T MRI. *NeuroImage* 170, 222–230. doi: 10.1016/j.neuroimage.2017.04.070

Bianciardi, M., Toschi, N., Edlow, B. L., Eichner, C., Setsompop, K., Polimeni, J. R., et al. (2015). Toward an in vivo neuroimaging template of human brainstem nuclei of the ascending arousal, autonomic, and motor systems. *Brain Connect.* 5, 597–607. doi: 10.1089/brain.2015.0347

Bokiniec, P., Shahbazian, S., McDougall, S. J., Berning, B. A., Cheng, D., Llewellyn-Smith, I. J., et al. (2017). Polysialic acid regulates sympathetic outflow by facilitating information transfer within the nucleus of the solitary tract. *J. Neurosci.* 37, 6558–6574. doi: 10.1523/JNEUROSCI.0200-17.2017

Brown, E. N., Lydic, R., and Schiff, N. D. (2010). General anesthesia, sleep, and coma. *N. Engl. J. Med.* 363, 2638–2650. doi: 10.1056/NEJMra0808281

Chamberlin, N. L. (2004). Functional organization of the parabrachial complex and intertrigeminal region in the control of breathing. *Respir. Physiol. Neurobiol.* 143, 115–125. doi: 10.1016/j.resp.2004.03.015

Choi, K.-D., and Kim, J.-S. (2018). Vascular vertigo: updates. *J. Neurol.* 266, 1835–1843. doi: 10.1007/s00415-018-9040-3

Cousins, S., Cutfield, N. J., Kaski, D., Palla, A., Seemungal, B. M., Golding, J. F., et al. (2014). Visual dependency and dizziness after vestibular neuritis. *PLoS One* 9:e105426. doi: 10.1371/journal.pone.0105426

Croxson, P. L., Forkel, S. J., Cerliani, L., and Thiebaut de Schotten, M. (2018). Structural variability across the primate brain: a cross-species comparison. *Cereb. Cortex* 28, 3829–3841. doi: 10.1093/cercor/bhx244

Damasceno, R. S., Takakura, A. C., and Moreira, T. S. (2014). Regulation of the chemosensory control of breathing by Kölliker-Fuse neurons. *Am. J. Physiol. Regul. Integr. Comp. Physiol.* 307, R57–R67. doi: 10.1152/ajpregu.00024.2014

Davern, P. J. (2014). A role for the lateral parabrachial nucleus in cardiovascular function and fluid homeostasis. *Front. Physiol.* 5:436. doi: 10.3389/fphys.2014.00436

Desikan, R. S., Ségonne, F., Fischl, B., Quinn, B. T., Dickerson, B. C., Blacker, D., et al. (2006). An automated labeling system for subdividing the human cerebral cortex on MRI scans into gyral based regions of interest. *NeuroImage* 31, 968–980. doi: 10.1016/j.neuroimage.2006.01.021

Destrieux, C., Fischl, B., Dale, A., and Halgren, E. (2010). Automatic parcellation of human cortical gyri and sulci using standard anatomical nomenclature. *NeuroImage* 53, 1–15. doi: 10.1016/j.neuroimage.2010.06.010

Dubuisson, M. P., and Jain, A. K. (1994). "A modified Hausdorff distance for object matching," in *Proceedings of 12th International Conference on Pattern Recognition*, Jerusalem, 566–568.

Dutia, M. B. (2010). Mechanisms of vestibular compensation: recent advances. *Curr. Opin. Otolaryngol. Head Neck Surg.* 18, 420–424. doi: 10.1097/MOO.0b013e32833de71f

Mahoney, A. E. J., Edelman, S., and D Cremer, P. (2013). Cognitive behavior therapy for chronic subjective dizziness: longer-term gains and predictors of disability. *Am. J. Otolaryngol.* 34, 115–120. doi: 10.1016/j.amjoto.2012.09.013

Fischl, B., Rajendran, N., Busa, E., Augustinack, J., Hinds, O., Yeo, B. T. T., et al. (2008). Cortical folding patterns and predicting cytoarchitecture. *Cereb. Cortex* 18, 1973–1980. doi: 10.1093/cercor/bhm225

Fuller, P., Sherman, D., Pedersen, N. P., Saper, C. B., and Lu, J. (2011). Reassessment of the structural basis of the ascending arousal system. *J. Comp. Neurol.* 519, 933–956. doi: 10.1002/cne.22559

García-Gomar, M. G., Strong, C., Toschi, N., Singh, K., Rosen, B. R., Wald, L. L., et al. (2019). *In vivo* probabilistic structural atlas of the inferior and superior colliculi, medial and lateral geniculate nuclei and superior olivary complex in humans based on 7 tesla MRI. *Front. Neurosci.* 13:764. doi: 10.3389/fnins.2019.00764

Gauriau, C., and Bernard, J.-F. (2002). Pain pathways and parabrachial circuits in the rat. *Exp. Physiol.* 87, 251–258. doi: 10.1113/eph8702357

Ghosal, S., Bundzikova-Osacka, J., Dolgas, C. M., Myers, B., and Herman, J. P. (2014). Glucocorticoid receptors in the nucleus of the solitary tract (NTS) decrease endocrine and behavioral stress responses. *Psychoneuroendocrinology* 45, 142–153. doi: 10.1016/j.psyneuen.2014.03.018

Godemann, F., Siefert, K., Hantschke-Brüggemann, M., Neu, P., Seidl, R., and Ströhle, A. (2005). What accounts for vertigo one year after neuritis vestibularis - anxiety or a dysfunctional vestibular organ? *J. Psychiatr. Res.* 39, 529–534. doi: 10.1016/j.jpsychires.2004.12.006

Greve, D. N., and Fischl, B. (2009). Accurate and robust brain image alignment using boundary-based registration. *NeuroImage* 48, 63–72. doi: 10.1016/j.neuroimage.2009.06.060

Heinrichs, N., Edler, C., Eskens, S., Mielczarek, M. M., and Moschner, C. (2007). Predicting continued dizziness after an acute peripheral vestibular disorder. *Psychosom. Med.* 69, 700–707. doi: 10.1097/PSY.0b013e318151a4dd

Indovina, I., Riccelli, R., Chiarella, G., Petrolo, C., Augimeri, A., Giofrè, L., et al. (2015). Role of the insula and vestibular system in patients with chronic subjective dizziness: an fMRI study using sound-evoked vestibular stimulation. *Front. Behav. Neurosci.* 9:334. doi: 10.3389/fnbeh.2015.00334

Indovina, I., Riccelli, R., Staab, J. P., Lacquaniti, F., and Passamonti, L. (2014). Personality traits modulate subcortical and cortical vestibular and anxiety responses to sound-evoked otolithic receptor stimulation. *J. Psychosom. Res.* 77, 391–400. doi: 10.1016/j.jpsychores.2014.09.005

Kaur, S., Pedersen, N. P., Yokota, S., Hur, E. E., Fuller, P. M., Lazarus, M., et al. (2013). Glutamatergic signaling from the parabrachial nucleus plays a critical role in hypercapnic arousal. *J. Neurosci.* 33, 7627–7640. doi: 10.1523/JNEUROSCI.0173-13.2013

Keil, B., Triantafyllou, C., Hamm, M., and Wald, L. (2010). "Design optimization of a 32-channel head coil at 7 T," in *Proceedings of the Annual Meeting of the International Society for Magnetic Resonance in Medicine*, Stockholm, 1493.

Kitahara, T., Takeda, N., Saika, T., Kubo, T., and Kiyama, H. (1997). Role of the flocculus in the development of vestibular compensation: immunohistochemical studies with retrograde tracing and flocculectomy using Fos expression as a marker in the rat brainstem. *Neuroscience* 76, 571–580. doi: 10.1016/s0306-4522(96)00374-0

Klein, A., Andersson, J., Ardekani, B. A., Ashburner, J., Avants, B., Chiang, M.-C., et al. (2009). Evaluation of 14 nonlinear deformation algorithms applied to human brain MRI registration. *NeuroImage* 46, 786–802. doi: 10.1016/j.neuroimage.2008.12.037

Klein, A., Ghosh, S. S., Avants, B., Yeo, B. T. T., Fischl, B., Ardekani, B., et al. (2010). Evaluation of volume-based and surface-based brain image registration methods. *NeuroImage* 51, 214–220. doi: 10.1016/j.neuroimage.2010.01.091

Linnman, C., Moulton, E. A., Barmettler, G., Becerra, L., and Borsook, D. (2012). Neuroimaging of the periaqueductal gray: state of the field. *NeuroImage* 60, 505–522. doi: 10.1016/j.neuroimage.2011.11.095

Matsumoto, I. (2013). Gustatory neural pathways revealed by genetic tracing from taste receptor cells. *Biosci. Biotechnol. Biochem.* 77, 1359–1362. doi: 10.1271/bbb.130117

Mello-Carpes, P. B., and Izquierdo, I. (2013). The Nucleus of the Solitary Tract → Nucleus Paragigantocellularis → *Locus Coeruleus* → CA1 region of dorsal hippocampus pathway is important for consolidation of object recognition memory. *Neurobiol. Learn. Mem.* 100, 56–63. doi: 10.1016/j.nlm.2012.12.002

Millan, M. J. (2002). Descending control of pain. *Prog. Neurobiol.* 66, 355–474.

Miyashita, T., and Williams, C. L. (2002). Glutamatergic transmission in the nucleus of the solitary tract modulates memory through influences on amygdala noradrenergic systems. *Behav. Neurosci.* 116, 13–21. doi: 10.1037/0735-7044.116.1.13

Myers, B., Scheimann, J. R., Franco-Villanueva, A., and Herman, J. P. (2017). Ascending mechanisms of stress integration: implications for brainstem regulation of neuroendocrine and behavioral stress responses. *Neurosci. Biobehav. Rev.* 74, 366–375. doi: 10.1016/j.neubiorev.2016.05.011

Naidich, T. P., Duvernoy, H. M., Delman, B. N., Sorensen, A. G., Kollias, S. S., and Haacke, E. M. (2009). *Duvernoy's Atlas of the Human Brain Stem and Cerebellum: High-Field MRI, Surface Anatomy, Internal Structure, Vascularization and 3 D Sectional Anatomy.* Berlin: Springer Science & Business Media.

Niblock, M. M., Kinney, H. C., Luce, C. J., Belliveau, R. A., and Filiano, J. J. (2004). The development of the medullary serotonergic system in the piglet. *Auton. Neurosci. Basic Clin.* 110, 65–80. doi: 10.1016/j.autneu.2003.10.004

NIDCD (2015). *2012-2016 NIDCD Strategic Plan.* Available at: https://www.nidcd.nih.gov/about/strategic-plan/2012-2016/2012-2016-nidcd-strategic-plan (accessed April 19, 2019)

Nigro, S., Indovina, I., Riccelli, R., Chiarella, G., Petrolo, C., Lacquaniti, F., et al. (2018). Reduced cortical folding in multi-modal vestibular regions in persistent postural perceptual dizziness. *Brain Imaging Behav.* 13, 798–809. doi: 10.1007/s11682-018-9900-6

Olszewski, J., and Baxter, D. (1954). *Cytoarchitecture of the Human Brain Stem.* Basel: Karger.

Passamonti, L., Riccelli, R., Lacquaniti, F., Staab, J. P., and Indovina, I. (2018). Brain responses to virtual reality visual motion stimulation are affected by neurotic personality traits in patients with persistent postural-perceptual dizziness. *J. Vestib. Res. Equilib. Orientat.* 28, 369–378. doi: 10.3233/VES-190653

Pattinson, K. T. S., Mitsis, G. D., Harvey, A. K., Jbabdi, S., Dirckx, S., Mayhew, S. D., et al. (2009). Determination of the human brainstem respiratory control network and its cortical connections in vivo using functional and structural imaging. *NeuroImage* 44, 295–305. doi: 10.1016/j.neuroimage.2008.09.007

Paxinos, G., and Huang, X. (1995). *Atlas of Human Brainstem.* Amsterdam: Elsevier.

Paxinos, G., Xu-Feng, H., Sengul, G., and Watson, C. (2012). "Chapter 8 - Organization of brainstem nuclei," in *The Human Nervous System (Third Edition)*, eds J. K. Mai, and G. Paxinos (San Diego, CA: Academic Press), 260–327. doi: 10.1016/B978-0-12-374236-0.10008-2

Reese, T. G., Heid, O., Weisskoff, R. M., and Wedeen, V. J. (2003). Reduction of eddy-current-induced distortion in diffusion MRI using a twice-refocused spin echo. *Magn. Reson. Med.* 49, 177–182. doi: 10.1002/mrm.10308

Reilly, S., and Trifunovic, R. (2001). Lateral parabrachial nucleus lesions in the rat: neophobia and conditioned taste aversion. *Brain Res. Bull.* 55, 359–366. doi: 10.1016/s0361-9230(01)00517-2

Riccelli, R., Indovina, I., Staab, J. P., Nigro, S., Augimeri, A., Lacquaniti, F., et al. (2017a). Neuroticism modulates brain visuo-vestibular and anxiety systems during a virtual rollercoaster task. *Hum. Brain Mapp.* 38, 715–726. doi: 10.1002/hbm.23411

Riccelli, R., Passamonti, L., Toschi, N., Nigro, S., Chiarella, G., Petrolo, C., et al. (2017b). Altered insular and occipital responses to simulated vertical self-motion in patients with persistent postural-perceptual dizziness. *Front. Neurol.* 8:529. doi: 10.3389/fneur.2017.00529

Rinaman, L. (2010). Ascending projections from the caudal visceral nucleus of the solitary tract to brain regions involved in food intake and energy expenditure. *Brain Res.* 1350, 18–34. doi: 10.1016/j.brainres.2010.03.059

Rinaman, L., and Dzmura, V. (2007). Experimental dissociation of neural circuits underlying conditioned avoidance and hypophagic responses to lithium chloride. *Am. J. Physiol. Regul. Integr. Comp. Physiol.* 293, R1495–R1503. doi: 10.1152/ajpregu.00393.2007

Ris, L., Capron, B., de Waele, C., Vidal, P. P., and Godaux, E. (1997). Dissociations between behavioural recovery and restoration of vestibular activity in the unilabyrinthectomized guinea-pig. *J. Physiol.* 500(Pt 2), 509–522. doi: 10.1113/jphysiol.1997.sp022037

Satpute, A. B., Wager, T. D., Cohen-Adad, J., Bianciardi, M., Choi, J.-K., Buhle, J. T., et al. (2013). Identification of discrete functional subregions of the human periaqueductal gray. *Proc. Natl. Acad. Sci. U.S.A.* 110, 17101–17106. doi: 10.1073/pnas.1306095110

Sclafani, A., Azzara, A. V., Touzani, K., Grigson, P. S., and Norgren, R. (2001). Parabrachial nucleus lesions block taste and attenuate flavor preference and aversion conditioning in rats. *Behav. Neurosci.* 115, 920–933. doi: 10.1037/0735-7044.115.4.920

Spector, A. C. (1995). Gustatory function in the parabrachial nuclei: implications from lesion studies in rats. *Rev. Neurosci.* 6, 143–175.

Staab, J. P., Balaban, C. D., and Furman, J. M. (2013). Threat assessment and locomotion: clinical applications of an integrated model of anxiety and postural control. *Semin. Neurol.* 33, 297–306. doi: 10.1055/s-0033-1356462

Staab, J. P., Rohe, D. E., Eggers, S. D. Z., and Shepard, N. T. (2014). Anxious, introverted personality traits in patients with chronic subjective dizziness. *J. Psychosom. Res.* 76, 80–83. doi: 10.1016/j.jpsychores.2013.11.008

Stejskal, E. O., and Tanner, J. E. (1965). Spin diffusion measurements: spin echoes in the presence of a time-dependent field gradient. *J. Chem. Phys.* 42, 288–292. doi: 10.1063/1.1695690

Varentsova, A., Zhang, S., and Arfanakis, K. (2014). Development of a high angular resolution diffusion imaging human brain template. *NeuroImage* 91, 177–186. doi: 10.1016/j.neuroimage.2014.01.009

Yarnykh, V. L. (2007). Actual flip-angle imaging in the pulsed steady state: a method for rapid three-dimensional mapping of the transmitted radiofrequency field. *Magn. Reson. Med.* 57, 192–200. doi: 10.1002/mrm.21120

Yushkevich, P. A., Piven, J., Hazlett, H. C., Smith, R. G., Ho, S., Gee, J. C., et al. (2006). User-guided 3D active contour segmentation of anatomical structures: significantly improved efficiency and reliability. *NeuroImage* 31, 1116–1128. doi: 10.1016/j.neuroimage.2006.01.015

Zuperku, E. J., Stucke, A. G., Hopp, F. A., and Stuth, E. A. E. (2017). Characteristics of breathing rate control mediated by a subregion within the pontine parabrachial complex. *J. Neurophysiol.* 117, 1030–1042. doi: 10.1152/jn.00591.2016